

# Perception-driven Formation Control of Airships

Eric Price<sup>1,2</sup>, Michael J. Black<sup>2</sup> and Aamir Ahmad<sup>1,2</sup>

**Abstract**—For tracking and motion capture (MoCap) of animals in their natural habitat, a formation of safe and silent aerial platforms, such as airships with on-board cameras, is well suited. However, unlike multi-rotors, airships are severely motion constrained and affected by ambient wind. Their orientation and flight direction are also tightly coupled. Therefore, state-of-the-art MPC-based formation control methods for perception tasks are not directly applicable for a team of airships. In this paper, we address this problem by first exploiting a periodic relationship between the airspeed of an airship and its distance to the subject. We use it to derive analytical and numeric solutions that satisfy the MoCap perception constraints. Based on this, we develop an MPC-based formation controller. We performed detailed analysis of our solution, including the effects of changing physical parameters (like angle of attack and pitch angle) on it. Extensive simulation experiments, comparing results for different formation sizes, different wind conditions and various subject speeds, are presented. A demonstration of our method on a real airship is also included. We have released all of our source code at <https://github.com/robot-perception-group/Airship-MPC>. A video describing our approach and results can be watched at [https://youtu.be/ihS0\\_VRD\\_kk](https://youtu.be/ihS0_VRD_kk)

## I. INTRODUCTION

Aerial motion capture (MoCap) of human and animal subjects, i.e., estimating the trajectory of their 3D positions, skeletal poses and body shape, using a team of aerial vehicles with on-board cameras, is a challenging task in various monitoring applications. For optimal aerial MoCap, in our previous work we developed an MPC-based [1] and a reinforcement learning-based [2] formation control method for multi-rotors. For human pose and shape estimation from multiple aerial images, our previous works include [3] and [4]. In these works, we have shown that observing an articulated subject, like a human, from multiple UAVs avoids self-occlusions in the subject and improves the accuracy of the MoCap estimates. In [1] and [2], we also established that optimal MoCap estimates can be achieved if i) the subject remains centered in the camera images of all UAVs, ii) the UAVs maintain a threshold distance to the subject within safety limits, and iii) the UAVs maintain a formation size-specific angular formation around the subject.

Both [1] and [4] assumed multi-rotor UAVs. These are not well suited for some subjects, such as animals in their natural habitat, due to their loud noise, low flight

<sup>1</sup>Institute of Flight Mechanics and Controls, The Faculty of Aerospace Engineering and Geodesy, University of Stuttgart, 70569 Stuttgart, Germany. (eric.price,aamir.ahmad)@ifr.uni-stuttgart.de

<sup>2</sup>Max Planck Institute for Intelligent Systems, 72076 Tübingen, Germany, mjb@tuebingen.mpg.de

We thank Yu Tang Liu, Pascal Goldschmid, Egor Iuganov, and student assistants at the Flight Robotic Group for their assistance with the flight experiments, as well as Pascal Goldschmid for extremely helpful discussions.

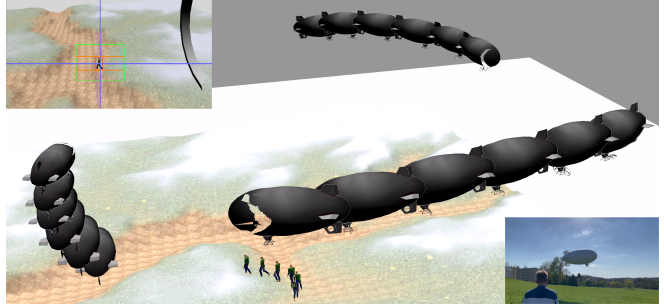


**Fig. 1:** A multi-exposure visualization of 3 simulated airships in a formation, tracking a moving person. The left-most airship climbs and drifts with the wind to keep the person in camera view, while the other two fly around on a curved trajectory. Top Left: Simulated view of one airship camera looking at the tracked person. Bottom Right: Our real blimp during an experiment.

time (battery) and safety-related concerns. Buoyant, helium-based, lighter than air vehicles (or airships) [5], [6] can address these concerns. These are relatively safe in terms of collision-related damage. Compared to multi-copters capable of carrying similar payloads, airships can have significantly longer flight times and considerably low noise levels.

Unfortunately, airship motion and control is substantially different from that of the multi-rotors. Therefore, the solutions developed in [1] and [4] are not directly applicable. Most airship designs need to remain in motion to be controllable. Their orientation and flight direction are also tightly coupled. For example, in order to climb, an airship typically needs to pitch up, which rotates the camera view around its lateral Y-axis, assuming a rigidly mounted camera. A directional change, on the other hand, triggers a roll around the airship’s longitudinal X-axis. Most importantly, classical airship designs allow movement only in the forward direction through the surrounding air, offset by a lateral angle of attack. While the global camera orientation could be decoupled from flight direction using gimbal-mounted cameras, these add additional weight and control complexity. Therefore, a solution is required for airship formation control for the task of aerial MoCap that i) does not need camera gimbals, and ii) adheres to the previously-mentioned optimal MoCap conditions. This is the core problem addressed in this paper.

One possible solution for the case of stationary subject and a single airship, is to mount the camera perpendicular to the forward direction of the airship, tilted downward at an angle, and let the airship orbit around the subject. For a formation of multiple airships, maintaining the same angular velocity by all airships would be a solution. However, for subjects moving with arbitrary and changing velocities, these solutions are not directly applicable.

The key contribution of this paper is that we show, both

theoretically and empirically, that subject-orbiting trajectories of airships can be generalized even to subjects in motion, while maintaining a perpendicular line-of-sight (LoS) to the subject and a prescribed angular separation between them. We achieve this by exploiting a periodic relationship between the airspeed of the airship and its distance to the subject. We also show how our method copes with wind, as both wind and subject motion result in equivalent relative velocity between the airship and the subject. Our further novel contributions include the following.

- We derive analytical solutions for a simplified 2D case (airships and the subject moving on the same plane) with simplified aerodynamics. From this, we derive boundary conditions on the subject velocity that allow possible orbit solutions under the constraints of maximum and minimum airship speeds.
- We then derive an approximate analytical solution in the full 3D case with realistic physics. Based on this, and a MoCap cost function, we develop a numeric solver for the formations. Utilizing this solver, we implement a fixed-time model predictive controller (MPC) for the formation control problem.

We evaluate our MPC in simulation experiments, where a formation of airships tracks a simulated subject (Fig. 1). We vary parameters such as wind, subject motion, and the number of vehicles in the formation and evaluate the MPC performance. Finally, we run the MPC on our real airship and let it orbit a simulated person on the ground. We made our source code available for the benefit of the community.

## II. RELATED WORKS

MPC has been extensively used for drone formation control [7], [1], [8], [9]. Most works on airship formation control, with [10] or without [11] MPC cover traditional formation types with pre-specified geometry. However, none considers centering a subject in the on-board camera's image or angular separation constraints with respect to a tracked subject.

Since the nonholonomic motion constraints of airships and fixed-wing aircrafts are similar enough to allow cross-application, we briefly overview some works in that field. Subject relative formations have been well studied for observation with fixed-wings, but primarily with straight downward facing cameras, where the vehicles loiter high above the subject [12], [13], [14], [15]. This greatly simplifies the formation control problem, while simultaneously limiting the observation angles to a top down birds-eye view, which is not well suitable for the MoCap task. In contrast, our approach can be employed for arbitrary observation angles and for subjects at the same altitude or even higher than the airship.

Orbiting trajectories for fixed-wing UAVs around a subject have been described in [16], where a Lyapunov function based vector field is designed to explicitly converge on an orbiting solution in a constant altitude plane. It maintains angular separation between vehicles and constant distance to the subject, but it does not consider vehicle orientation and camera viewing angles relative to the subject. The Lyapunov

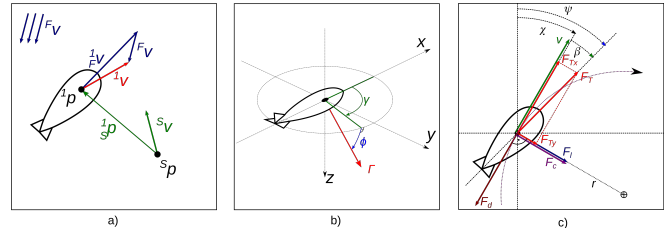


**Fig. 2:** a) Absolute and relative position and velocity of airship 1 near subject  $S$ . b) Camera angle in the blimp body frame. c) Forces on an airship on a curved trajectory, subject to aerodynamic lift and drag.

function based approach is sensitive to starting conditions and can not easily be extended to maintain additional constraints. Our optimization based approach not only converges on steady state solutions, but also optimizes the transition phases for optimal subject coverage, considers motion in 3D space and can enforce constraints on both state and control inputs.

## III. METHODOLOGY

### A. Notations

In the world frame, the velocity of airship  $n \in [1 \dots N]$  at time  $t$  is given as  ${}^n v_t = [{}^n v_{xt}, {}^n v_{yt}, {}^n v_{zt}]^\top$  and its horizontal speed is given as  ${}^n v_{ht} = \| [{}^n v_{xt}, {}^n v_{yt}] \|$ . The wind/fluid vector is given as  ${}^F v$ . The velocity of the subject is given as  ${}^S v$ , assuming it is moving on the 2D ground plane. The position of airship  $n$  and subject  $S$  at time  $t$  are given as  ${}^n p_t$  and  ${}^S p_t$ , respectively. We use a left subscript to denote a reference frame different from world frame, e.g., the velocity of airship  $n$  at time  $t$  relative to the fluid  $F$  is given as  ${}^F v_t = {}^n v_t - {}^F v$  and the position of airship  $n$  relative to subject  $S$  is given as  ${}^S p_t = {}^n p_t - {}^S p_t$  (Fig. 2a).

All positions and velocities are oriented North-East-Down, unless specified otherwise. In airship body frame we consider  $x$  forward,  $y$  rightward and  $z$  downward. The orientation of airship  $n$  at time  $t$  is given as  ${}^n \Theta_t = [{}^n \varphi_t, {}^n \theta_t, {}^n \psi_t]^\top$ , with components roll  ${}^n \varphi_t$ , pitch  ${}^n \theta_t$  and yaw  ${}^n \psi_t$ . The horizontal motion direction of airship  $n$  in the fluid is given as

$${}^F \chi_t = \text{atan}2 \left( \frac{{}^n v_{yt}}{{}^n v_{xt}} \right). \quad (1)$$

We write  ${}^n \dot{\psi}_t$  for the yaw rate and  ${}^n \dot{\chi}_t$  for the turn rate of airship  $n$  at time  $t$ . We define the formation state of  $N$  airships, at time  $t$  as

$$\mathbf{X}_t = [{}^S X_t, {}^1 X_t, \dots, {}^N X_t]^\top, \quad (2)$$

consisting of subject state  ${}^S X_t = [{}^S p_t]$  and airship states  ${}^n X_t = [{}^n p_t, {}^n v_t, {}^n \Theta_t]^\top$  for all airships  $n \in [1 \dots N]$ .

### B. Problem Statement

Let us assume a team of  $N$  airships, each with a body-fixed camera, tracking a moving subject  $S$ . Let us also assume that the camera's fixed azimuth and elevation angles with respect to its carrier airship is given as  $\gamma$  and  $\phi$ , respectively, and represented jointly as  $\Gamma = [\gamma, \phi]$ . Our goal is to control the airship's acceleration  ${}^n \dot{v}$  and yaw rate  ${}^n \dot{\psi}_t$ , such that the following conditions are met.

- 1)  $S$  remains centered in the camera view for all  $n \in [1 \dots N]$ , a MoCap accuracy specific requirement [2].
- 2) The angles subtended by any two airships  $n, m$ , with respect to the subject  $S$  remains equal to a defined preset that is optimal for minimizing the joint state estimation uncertainty. In [1], it was shown that an angle of  $\frac{2\pi}{N}$  for  $N > 2$  and  $\frac{\pi}{2}$  for  $N = 2$  is optimal.
- 3) Other input and state constraints. We assume that in order to remain maneuverable, each airship must fly above a minimum airspeed  $v_{\min}$  and, due to drag and finite thrust, cannot exceed  $v_{\max}$  such that

$$v_{\min} \leq \|{}^F v_t\| \leq v_{\max}. \quad (3)$$

### C. Planar Airship Orbits in 2D

For our primary analysis, we consider a system with the following simplifications: i) movement and rotation in a 2D X/Y plane, ii) movement only in the heading direction ( ${}^n \psi_t = {}^n \chi_t$ ). If airship  $n$  moves at velocity  $\|{}^F v_t\| > v_{\min}$ , while the subject is not moving relative to the fluid ( $\|{}^S v\| = 0$ ), then the only stable solution to keep the subject centered in camera view is i) to mount the camera perpendicular to the motion direction with  $\gamma = \pm \frac{\pi}{2}$  and ii) to orbit on a curved, tangential path with constant radius

$${}^S r_t = \|{}^S p_t\|. \quad (4)$$

This satisfies the equation of circular motion

$${}^S r_t = \frac{\|{}^n v_t\|}{{}^n \dot{\psi}_t}, \quad (5)$$

with rotation speed  $\|{}^n v_t\|$  and rotation rate  ${}^n \dot{\psi}_t$ . Since  ${}^n \dot{\psi}_t$  can be controlled, this can be done for arbitrary radii regardless of velocity constraints.

If the subject is moving ( $\|{}^S v\| \neq 0$ ), it is still possible to orbit around  $S$  while keeping it centered in the camera view. We exploit symmetry in order to illustrate this in an intuitive way and assume, without limiting generality, that the subject is moving along the negative X axis with  ${}^n \dot{\psi}_t > 0$  and  $\gamma = \frac{\pi}{2}$ . To keep the subject centered in the camera, the speed of airship  $n$  must always match the subject velocity component perpendicular to the camera axis. Since the airship is also orbiting, this adds to the rotation speed at the current radius. Thus  $\|{}^F v_t\|$  should now be

$$\|{}^F v_t\| = {}^S r_t {}^n \dot{\psi}_t - \cos({}^n \psi_t) \|{}^S v\|. \quad (6)$$

Since by assumption (in this subsection only) the airship can only fly in the direction it is pointing, the distance to the subject, which is the current orbit radius, will change as

$${}^S \dot{r}_t = \sin({}^n \psi_t) \|{}^S v\|. \quad (7)$$

By integration, we introduce constant  $r_0$  as a base radius. Thus  ${}^S r_t$  can be given as

$${}^S r_t = r_0 - \cos({}^n \psi_t) \frac{\|{}^S v\|}{{}^n \dot{\psi}_t}. \quad (8)$$

Inserting (8) in (6), we get

$$\|{}^F v_t\| = {}^n \dot{\psi}_t r_0 - 2 \cos({}^n \psi_t) \|{}^S v\|, \quad (9)$$

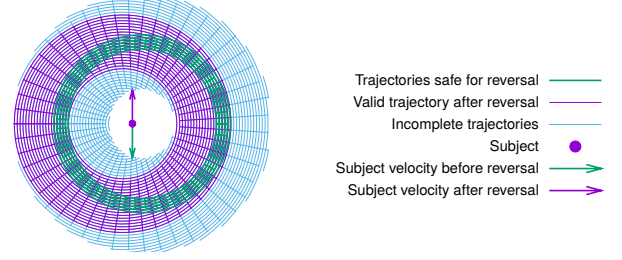


**Fig. 3:** Subject velocity reversal: Orbital space around moving subject for a fixed yaw rate and airship velocity constraints  $v_{\min} \leq \|{}^F v\| \leq v_{\max}$ , with visualization of the effect of reversal of  ${}^S v$  direction. For any  ${}^n \psi_t$ , the innermost valid trajectory reaches  $v_{\min}$  when flying opposite to the subject, the outermost approaches  $v_{\max}$  when flying parallel to the subject. A trajectory is safe under reversal (green), if every point on the trajectory lies on a closed and valid purple trajectory. Trajectories in blue can not be followed without violating constraints (blank areas).

from which we calculate minimal and maximal airspeed during the orbit as

$$\min(\|{}^F v_t\|) = {}^n \dot{\psi}_t r_0 - 2 \|{}^S v\| \quad (10)$$

and

$$\max(\|{}^F v_t\|) = {}^n \dot{\psi}_t r_0 + 2 \|{}^S v\|, \quad (11)$$

for a desired yaw rate  ${}^n \dot{\psi}_t$  and base radius  $r_0$ , i.e., the distance to the stationary subject or the average distance to a moving subject over one orbit.

Multiple airships in a formation, i.e.,  $N > 1$ , can maintain the angular constraints (2nd constraint in Subsec. III-B) only when  ${}^n \dot{\psi}_t$  is the same for all airships. For physically achievable (3) orbits that satisfy all the required perception constraints (Subsec. III-B),

$$\min(\|{}^F v_t\|) \geq v_{\min} \quad \text{and} \quad \max(\|{}^F v_t\|) \leq v_{\max}, \quad (12)$$

must hold.

If two airships  $m, n$  are opposed by  $\pi$  on the same orbit, at  ${}^m \psi_t = 0$  and  ${}^n \psi_t = \pi$ , the worst case scenario is that the velocity of airship  $m$ , given by (10), approaches  $v_{\min}$  and the velocity of airship  $n$ , given by (11), approaches  $v_{\max}$ , both simultaneously. Solving for the subject velocity using (10) and (11) at this point leads to

$$\|{}^S v\| = \frac{(v_{\max} - v_{\min})}{4}. \quad (13)$$

Consequently, the maximum magnitude of the subject velocity for which the whole orbit satisfies all the required conditions (Subsec. III-B) is given as

$$\|{}^S v\| \leq \frac{(v_{\max} - v_{\min})}{4}. \quad (14)$$

*Stability under reversal:* Although we consider the subject velocity as constant, we can also determine robustness of this approach to changes in  ${}^S v$ . The worst-case scenario is the sudden reversal of the fluid- or subject-motion which, as shown in Fig. 3, inverts the offset of the trajectory relative to the subject. The airship might now be on an invalid (blue) orbit. Continuing on that trajectory would then violate (3). However, a family of orbits exist, for which the whole orbit, including minimum and maximum is always on a safe

trajectory after reversal, as displayed in Fig. 3 in green. Analogous to (14), it can be shown that trajectories safe under single reversal are guaranteed to exist if

$$\|{}^S_F v\| \leq \frac{(v_{\max} - v_{\min})}{8} \quad (15)$$

and generally safe trajectories for  $q$  consecutive reversals spaced  $\frac{1}{2}$  orbit apart are guaranteed to exist if

$$\|{}^S_F v\| \leq \frac{(v_{\max} - v_{\min})}{4(q+1)}. \quad (16)$$

In Summary, the analytic solution with the 2D assumptions for our problem statement (Subsec. III-B), is given by (8) subject to constraint (14).

#### D. Airship Orbits in 3D with Realistic Physics

A realistic airship model must take aerodynamic forces into account. The hull of an airship, as depicted in Fig. 2c is subject to lift and drag forces [17] and can be modeled as an airfoil. Below we model the following physical parameters.

1) *Lateral angle of attack*: In a real airship  ${}^n\psi_t \neq {}^n\chi_t$  unless the airship flies in a straight line. To fly in a curve, a centripetal force  $F_t$  needs to act on the airship. This force is a combination of the lateral engine thrust vector and aerodynamic lift. Both force components are a function of the lateral angle of attack  ${}^n_F\beta_t$  [17], given as

$${}^n_F\beta_t = {}^n\psi_t - {}^n_F\chi_t. \quad (17)$$

For small  ${}^n_F\beta_t$  we can approximate a linear relationship between  ${}^n_F\beta_t$  and the lateral force. As the airship rotates with  ${}^n\dot{\psi}_t$ ,  ${}^n_F\beta_t$  increases until the lateral acceleration approaches centripetal acceleration

$${}^n a_{ct} = \|{}^n_F v_t\| {}^n \dot{\psi}_t. \quad (18)$$

At this point  ${}^n_F \dot{\chi}_t = {}^n \dot{\psi}_t$  and  ${}^n \dot{\beta}_t = 0$ . Thus, for a fixed yaw rate  ${}^n\dot{\psi}_t$  and for sufficient airspeed  $\|{}^n_F v_t\| \geq v_{\min}$  we can approximate as

$${}^n_F\beta_t \approx \frac{{}^n\dot{\psi}_t}{c_l \|{}^n_F v_t\|}, \quad (19)$$

where  $c_l$  is a system-specific coefficient, representing the combined effect of the airship lift and drag [17].

2) *Changes in velocity*: If the airship is undergoing acceleration  ${}^n_F a_s$  in the direction of motion  ${}^n_F \chi_t$ , then  $\|{}^n_F v_t\|$ , given as

$$\|{}^n_F v_t\| = \|{}^n_F v_{t0}\| + t \|{}^n_F a_s\|. \quad (20)$$

To calculate

$${}^n_F v_t = \|{}^n_F v_t\| \begin{bmatrix} \cos({}^n_F \chi_t) \\ \sin({}^n_F \chi_t) \end{bmatrix}, \quad (21)$$

we determine

$${}^n_F \chi_t = {}^n\psi_t - {}^n_F\beta_t, \quad (22)$$

as a function of  ${}^n\dot{\psi}_t$  by plugging (19) in (22) and obtain

$${}^n_F \chi_t \approx {}^n\psi_t - \frac{{}^n\dot{\psi}_t}{c_l \|{}^n_F v_t\|}. \quad (23)$$

3) *Roll angle*: Most airships are passively stable in roll and have their center of mass underneath the center of lift and buoyancy. Consequently, they self-orient according to the sum of gravity and centripetal acceleration. We can approximate the roll angle of airship  $n$  at time  $t$  as

$${}^n\varphi_t \approx \tan\left(\frac{{}^n_F \dot{\chi}_t \|{}^n_F v_t\|}{g}\right), \quad (24)$$

where  $g \approx 9.81 \frac{\text{m}}{\text{s}^2}$  is earth gravity. In fixed wing aircraft the same formula describes a *coordinated turn* [17].

4) *Altitude*: For altitude changes, we assume that the airship can change its vertical speed arbitrarily and independent of its horizontal motion, within limits [6]. For the analytical solution, the necessary altitude  $(-{}^n_S p_{zt})$  above  $S$  to maintain the subject centered in the camera view is approximated based on radius  ${}^n_S r_t$  and camera elevation  $\phi$  (Fig. 2b) as

$$-{}^n_S p_{zt} \approx \frac{\tan({}^n\varphi_t - \phi)}{{}^n_S r_t}. \quad (25)$$

While this analytical solution ignores the effect of the airships pitch angle  ${}^n\theta_t$ , we explicitly consider it later in the numeric solution (Subsec. III-E).

5) *Pitch angle*: We approximate pitch angle  ${}^n\theta_t$  as

$${}^n\theta_t \approx \tan\left(\frac{-{}^n_F v_{zt}}{{}^n_F v_{ht}}\right). \quad (26)$$

In summary, one approximate analytical solution for airship orbits in 3D for our problem statement (Subsec. III-B) can be obtained by combining (8), (24) and (25), however the effect of changes in  ${}^n\theta_t$  is not reflected in this analytical solution. In the numeric solution (Subsec. III-E), we empirically show that changes in  ${}^n\theta_t$  make the orbits less eccentric than in (8).

#### E. Optimization Formulation for Numeric Solution

We can find an optimal trajectory for a formation starting state  $\mathbf{X}_0$ , by minimizing a cost function  $C$  given as

$$C = \sum_{t,n} (k_c {}^n E_{ct} + k_f {}^n E_{ft}), \quad (27)$$

subject to constraints

$$v_{\min} \leq \|{}^n_F v_t\| \leq v_{\max} \quad \text{and} \quad \|{}^n_F v_{zt}\| \leq v_{v\max}. \quad (28)$$

$k_c {}^n E_{ct}$  keeps the person  $S$  centered in the camera images, while  $k_f {}^n E_{ft}$  maintains angular separation between the airships around  $S$ . Here

$${}^n E_{ct} = \left\| \begin{bmatrix} k_d \\ 1 \\ 1 \end{bmatrix} \left( \begin{bmatrix} d_c \\ 0 \\ 0 \end{bmatrix} - {}^n \mathbf{R}_t (-{}^n_S p_t) \right) \right\|^2, \quad (29)$$

${}^n \mathbf{R}_t$  is the rotation matrix combining  $\Gamma$  and  ${}^n \Theta_t$  for a projection of  $S$  into the camera coordinate system of airship  $n$ ,  $k_d$  is a weight for the distance term, and  $d_c$  is the optimal camera distance. As shown in [1], a formation is optimal for minimizing joint uncertainty in state estimate when equally spaced for 3 or more vehicles, but at  $90^\circ$  to each other for 2 vehicles. This is achieved with

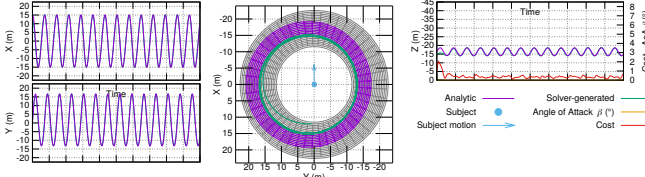


**Fig. 4:** Orbital space around moving subject for a fixed yaw rate  ${}^n\dot{\psi}_t = \text{const}$  and velocity constraints on the airship  $v_{\min} \leq \|{}^n\dot{v}_t\| \leq v_{\max}$ . Here, we assume  $c_l \rightarrow \infty$ , which implies  ${}^n\dot{\psi}_t = {}^n\dot{\chi}_t$  and  ${}^n\beta_t = {}^n\theta_t = 0$ . This allows an analytic orbital solution set, shown in purple in the center plot. Orbita closer to the subject violate  $v_{\min}$  while those further away violate  $v_{\max}$ . Increases in  ${}^n\dot{\psi}_t$  causes a scale reduction of the solution space, while decreases in  ${}^n\dot{\psi}_t$  result in larger orbits. The green trajectory is a numeric approximation of the optimal solution, minimizing the cost  ${}^nE_{ft}$ , displayed in red. The green trajectory closely matches the specific analytic solution in Subsec. III-C for  $\min(\|{}^n\dot{v}_t\|) = v_{\min}$ , displayed in purple in the two left plots.

$${}^nE_{ft} = \begin{cases} \sum_{m=1}^N \left( \frac{\pi}{2} - \arccos(|-{}^n\dot{p}_t| \cdot |{}^m\dot{p}_t|) \right)^2 & \text{for } N = 2 \\ \sum_{m=1}^N \max(0, \frac{2\pi}{N} - \arccos(|-{}^n\dot{p}_t| \cdot |{}^m\dot{p}_t|))^2 & \text{for } N \geq 3. \end{cases} \quad (30)$$

For  $N \geq 3$ ,  ${}^nE_{ft}$  penalizes airships that are separated by less than the desired angular distance for an evenly spaced formation  $\frac{2\pi}{N}$ . This has a repulsive effect and optimizes for equal spacing without enforcing any specific order.

We solve for control input  $U$  at time  $t$ , consisting of vehicle controls  ${}^nU_t$ , with

$$U_t = \begin{bmatrix} {}^1U_t, \dots, {}^NU_t \end{bmatrix} \quad \text{and} \quad {}^nU_t = \begin{bmatrix} {}^n\dot{\psi}_t, {}^n\dot{v}_{ht}, {}^n\dot{v}_{zt} \end{bmatrix}. \quad (31)$$

We define the discrete time state transition consisting of subject state transition and state transitions for all airships, with

$$\mathbf{X}_{t+\Delta t} = \begin{bmatrix} {}^S X_{t+\Delta t}, {}^1 X_{t+\Delta t}, \dots, {}^N X_{t+\Delta t} \end{bmatrix}^\top. \quad (32)$$

The subject state transition is given as

$${}^S X_{t+\Delta t} = \begin{bmatrix} {}^S p_t + \Delta t {}^S v \end{bmatrix}. \quad (33)$$

The airship state transition is given by

$${}^n X_{t+\Delta t} = [{}^n p_{t+\Delta t}, {}^n v_{t+\Delta t}, {}^n \Theta_{t+\Delta t}]^\top, \quad (34)$$

where  ${}^n p_{t+\Delta t}$  is calculated as

$${}^n p_{t+\Delta t} = {}^n p_t + ({}^n v_t + {}^F v) \Delta t. \quad (35)$$

${}^n v_{t+\Delta t}$  is calculated as

$${}^n v_{t+\Delta t} = {}^F v_{t+\Delta t} + {}^F v, \quad (36)$$

where

$${}^F v_{t+\Delta t} = \begin{bmatrix} ({}^F v_{ht} + {}^n \dot{v}_{ht} \Delta t) \cos({}^n \dot{\chi}_{t+\Delta t}) \\ ({}^F v_{ht} + {}^n \dot{v}_{ht} \Delta t) \sin({}^n \dot{\chi}_{t+\Delta t}) \\ {}^n v_{zt} + {}^n \dot{v}_{zt} \Delta t \end{bmatrix}. \quad (37)$$

${}^n \Theta_{t+\Delta t}$  is computed as

$${}^n \Theta_{t+\Delta t} = \begin{bmatrix} {}^n \varphi_{t+\Delta t} \\ {}^n \theta_{t+\Delta t} \\ {}^n \psi_t + {}^n \dot{\psi}_t \Delta t \end{bmatrix}. \quad (38)$$

In the above equations,  ${}^n \chi_{t+\Delta t}$ ,  ${}^n \varphi_{t+\Delta t}$  and  ${}^n \theta_{t+\Delta t}$  are calculated according to (23), (24) and (26), respectively.

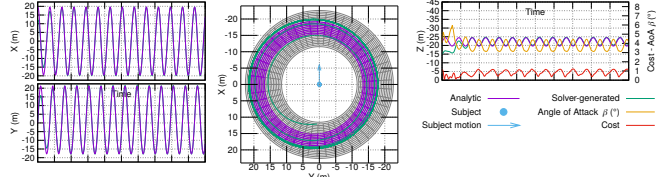


**Fig. 5:** Analysis of the effect of  ${}^n\beta_t$ . Orbital space around a moving subject for a fixed yaw rate and velocity constraints on the airship  $v_{\min} \leq \|{}^n\dot{v}_t\| \leq v_{\max}$ .  ${}^n\theta_t$  is assumed zero. The purple trajectories in the two left plots are the specific analytic solution from Subsec. III-C, shown for  $\max(\|{}^n\dot{v}_t\|) = v_{\max}$ . The green trajectory is a numeric approximation, but taking AoA  ${}^n\beta_t$  into account for a  $c_l$  of 0.8. At a sensor angle of  $\gamma = \frac{\pi}{2}$  this angular offset forces the airship on an outward spiral. Once the maximum constraint-satisfying distance is reached, the airship can no longer maintain the subject centered in the camera view, as seen in the non-zero cost (red).

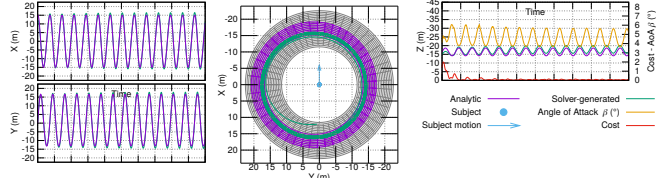


**Fig. 6:** Analysis of the effect of  ${}^n\beta_t$ . The same plot as in Fig. 5, but we now assume a camera azimuth of  $\gamma = 87^\circ$ . This small offset of  $3^\circ$  allows the solver to converge to a solution only slightly further out than  $\min(\|{}^n\dot{v}_t\|) = v_{\min}$ , at which the effects of AoA  ${}^n\beta_t$  are fully compensated over a full orbit, allowing the subject to remain centered in the camera image within tight tolerances. This solution is stable, as closer orbits cause a higher AoA, resulting in an outwards spiral, while larger orbits enforce an inward spiral, both re-converging to an optimal solution. The purple trajectories in the two left plots show the analytic solution with the smallest radius, with  $\min(\|{}^n\dot{v}_t\|) = v_{\min}$ .

## F. Model Evaluation

We implemented the optimization problem described above (Subsec. III-E) using OpEn/PANOC [18], [19]. To increase the accuracy at large  $\Delta t$ , we use the Runge Kutta method to integrate over  $\int {}^n v_t \delta t$  to estimate  ${}^n p_t$  in (35).

A single airship trajectory, optimized using the model in Sec. III-E converges to the analytical optimal solution described in Sec. III-C as shown in Fig. 4, if  ${}^n\beta_t$  and  ${}^n\theta_t$  are set to 0 and  ${}^n\dot{\psi}_t$  is set constant. If the starting state is not on the optimal trajectory, there is a short transitional phase, where the cost is minimal but not zero.  $k_d$  is set to 0 for this evaluation to compute the most optimal trajectory, without regard to the distance between the airship and subject  $S$ .

As shown in Fig. 5, a non-zero lateral angle of attack  ${}^n\beta_t$  results in a trajectory, where the person is not centered in the camera, but is skewed by approximately  ${}^n\beta_t$ .  ${}^n\beta_t$  is smaller at higher airspeed, as such the numeric solution approaches the largest radius possible within constraints. To compensate for this effect, one solution is to adjust the camera azimuth  $\gamma$  (Fig 2). An intuitive correction would be  $\gamma = \frac{\pi}{2} - \text{mean}({}^n\beta_t)$ , so that the average would be zero. This mean depends not only on the model parameters but also on the mean velocity, which in turn depends on the orbit radius. We can estimate it by applying (19) on a circular orbit with the same parameters. In Fig. 5,  ${}^n\beta_t$  oscillates between  $3^\circ$  and  $4.5^\circ$ .

Figure 6 shows that setting  $\gamma = 87^\circ$  solves this problem and allows an optimal solution close to the minimum radius.

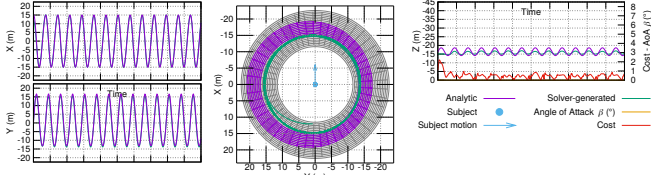


**Fig. 7:** Analysis of the effect of  ${}^n\theta_t$ . AoA  ${}^n\beta_t$  is assumed 0. The numeric solution (green) takes  ${}^n\theta_t$  into account. The resulting optimal trajectory is shallower than the analytic solution, but shares the same minimum radius. The maximum radius is however significantly reduced, implying that there could be viable orbits in 3D with  $\|{}^S_F v\| > \frac{1}{4}(v_{\max} - v_{\min})$ .

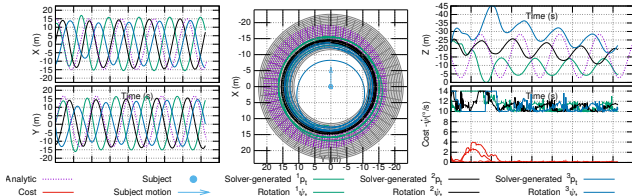


**Fig. 8:** Numerically solved optimal formation of 3 airships around a moving subject. Trajectories have a non-optimal starting point, leading to some non-optimal subject centering in order to converge on a global optimal formation within the first  $1\frac{1}{2}$  orbits. The red plot shows only the cost term  ${}^nE_{ct}$ .

Intuitively, a larger orbit results in higher velocities and a smaller  ${}^n\beta_t$ . When  $\gamma > \frac{\pi}{2} - \text{mean}({}^n\beta_t)$ , the airship needs to then fly an inward spiral to keep the subject centered in view. Similarly, a too tight orbit will lead to larger lateral angle of attack with  $\gamma < \frac{\pi}{2} - \text{mean}({}^n\beta_t)$ . Consequently, the formation will naturally converge on an orbit with  $\gamma = \frac{\pi}{2} - \text{mean}({}^n\beta_t)$ . This is not a limitation for our approach, as we still have  ${}^n\dot{\psi}_t$  as a controllable variable to change the desired distance to the subject.

Figure 7 shows the effect of  ${}^n\theta_t$  with a camera angled  $\phi = -45^\circ$  downwards. Intuitively, when the nose of the airship raises in a climb, which is the case whenever the radius  ${}^nS_{rt}$  grows (25), the camera looks further ahead. Compensating this to keep subject  $S$  in view, enforces a sharper turn, diminishing the  ${}^nS_{rt}$  increase. Symmetrically, when descending during shrinking  ${}^nS_{rt}$ , the camera looks behind. Both effects reduce the change in  ${}^nS_{rt}$ . As the change in radius  ${}^nS_{rt}$  is now less pronounced as in the analytic 2D case in Subsec. III-C, the upper bound for the subject velocity (14) becomes relaxed.

As shown before, orbiting solutions are guaranteed to exist if  $\|{}^S_F v\| \leq \frac{1}{4}(v_{\max} - v_{\min})$ . However, with the change in  ${}^n\theta_t$ , solutions might exist for  $\|{}^S_F v\| > \frac{1}{4}(v_{\max} - v_{\min})$ , but we have no analytical solution for the exact boundary, which depends on parameters  $\gamma$ ,  $\phi$ ,  ${}^n\beta_t$ ,  $c_l$ ,  ${}^n\varphi_t$  and  ${}^n\dot{\psi}_t$ .

Finally we apply the solver to compute optimal formation trajectories for 3 airships. In order to allow airships to adjust their relative angles to subject  $S$ , we no longer pre-specify the yaw rate  ${}^n\dot{\psi}_t$ , but allow the solver to adjust  ${}^n\dot{\psi}_t$  within new constraints  $\dot{\psi}_{\min} \leq {}^n\dot{\psi}_t \leq \dot{\psi}_{\max}$  to converge to an optimal multi airship formation, shown in Fig. 8. The constraints are identical for all airships. As cost weight  $k_f > 0$  is now in effect, the optimal solution is a trade-off between  ${}^nE_{ct}$  and  ${}^nE_{f_t}$ .

## IV. IMPLEMENTATION, EXPERIMENTS AND RESULTS

### A. Implementation and Experimental Setup

We implement the model in sec III-E as a non linear MPC for real airships. For this we reduce the planning horizon to approximately  $\frac{1}{3}$  orbit. This planning horizon is long enough to conduct a  $180^\circ$  if necessary, e.g., in case of sub-optimal starting conditions or to avoid collisions. Additional control constraints are enforced to limit the change in  ${}^n\dot{\psi}_t$  in each timestep, and state constraints such as minimum-height to avoid ground contact. We also added additional non-convex constraints to enforce sufficient distances between airships at all times and prevent collisions between them and possible static obstacles. In the absence of static obstacles, any solution close to the optimum has the airships maximally spread out due to cost term (30), which naturally forms a large convex corridor that optimal orbits reside in.

We modify the open source airship controller in [6] to take  ${}^n\dot{\psi}_t$ ,  ${}^F v_{ht}$  and  ${}^F v_{zt}$  as control inputs directly. We can measure  ${}^F v_{ht}$  using a pitot probe and  ${}^nX_t$  and  ${}^n\dot{\psi}_t$  using GPS and inertial sensors, which allows us to estimate wind vector  ${}^F v_t$  by inverting (37) with a numerical approximation method. We employ the cooperative perception framework of AirCap [4] to estimate  ${}^S X_t$  from  ${}^{1\dots N} X_t$  and visual detection in the camera images using a single shot detector neural network [20] and a distributed Bayesian filter. We assume  ${}^F v$  and  ${}^S v$  constant over the planning horizon. We estimate the model specific parameters  $c_l$  for a real airships by measuring  ${}^n\beta_t$  during a constant rate turn (19). With this, we can use our MPC to control a real or simulated airship. With a horizon of 10 timesteps and  $\Delta t = 1.25\text{s}$ , the OpEN engine typically converges within  $\sim 20\text{ms}$ , which is fast enough for real time application.

For all experiments, we set  $k_c = 1$ ,  $k_d = 0.6$ ,  $d_c = 15\text{m}$ ,  $k_f = 100$  as optimization weights. Camera and vehicle parameters for the simulated airships were  $\gamma = 82^\circ$ ,  $\phi = -30^\circ$ ,  $c_l = 0.24$ . The state constraints were set to  $v_{\min} = 0.5\frac{\text{m}}{\text{s}}$ ,  $v_{\max} = 4.0\frac{\text{m}}{\text{s}}$ ,  $v_{\max} = 1.5\frac{\text{m}}{\text{s}}$ ,  $\dot{\psi}_{\min\max} = \pm 18^\circ$ , allowing both left and right turns.

### B. Experiment Description and Evaluation Metrics

In Experiment 1, we evaluate different formation sizes up to  $N = 6$  airships around a stationary subject, with constant wind of  ${}^F v = 0.6\frac{\text{m}}{\text{s}}$ . In Experiment 2, we investigate the effect of wind and wind gusts with  $N = 3$  airships. In Experiment 3, we investigate the effect of subject motion, including sudden turns, with and without wind. Finally, in Experiment 4, we evaluate our MPC in an outdoor environment with a real airship but a simulated stationary subject.

In experiments 1–3, we evaluate 4 different metrics.

- 1) The visual tracking accuracy, which measures how well the estimated subject position, given as  ${}^S p_t$ , agrees with the ground-truth  ${}^S_{\text{GT}} p_t$  in simulation, calculated as  $\|{}^S p_t - {}^S_{\text{GT}} p_t\|$ .
- 2) Tracking uncertainty, measured as the trace of the covariance matrix of the subject position estimate.

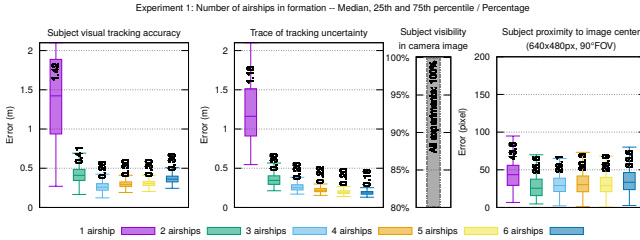


Fig. 9: Experiment 1: Variation of Formation Size.

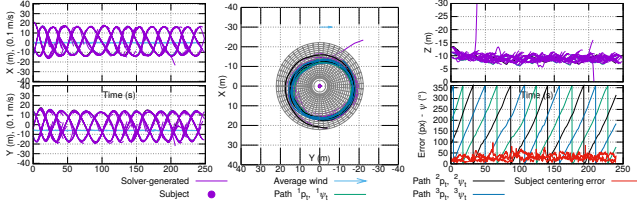


Fig. 10: Experiment 1: Simulated 3 airship flight. The 2 left and top right plots show the position of 3 airships in green, black and dark blue. The individual MPC trajectories for each time horizon are shown as thin purple lines. The wind estimate is light blue. The center plot shows airship positions and MPC trajectories in the x/y plane. The bottom right plot shows the distance of the subject from the camera center for all 3 airships in red, and the orientation  ${}^n\psi_t$  in green, black and dark blue.

- 3) Subject visibility, which is the percentage of video frames that have the subject in the field of view (FOV). The subject is considered in FOV if its projected center point is distanced less than half the camera resolution from the image center point. For this, the camera is simulated as a pinhole projection with  $640 \times 480$  pixels resolution and  $90^\circ$  camera FOV.
- 4) The proximity to the image center, measured as the distance in pixels of the subject center to the camera image center.

In experiment 4, since no tracking takes place, we use only iii) and iv), but in addition we qualitatively observe, whether the actually flown trajectory matches the solver generated trajectories.

### C. Experiment 1 - Formation Size

Figure 9 summarizes the effect of formation size on the tracking formation with  $N = 1, 2, 3, 4, 5$  and  $6$ . All evaluations were conducted with wind speed  $\|{}^F v\| = 0.6 \frac{m}{s}$ . For  $N = 1$  there is a larger tracking error, which is expected since a single airship cannot reliably estimate the depth from a single camera image. For  $N \geq 2$  the tracking error is significantly smaller than for  $N = 1$  and remains consistently low for up to 6 airships. The tracking uncertainty also shows a similar trend, decreasing with each additional airship in the formation. All formations managed to maintain sight of the subject 100% of the time, with the distance to the camera center averaging around 30px and never exceeding 100px.

Figure 10 shows the trajectories in the 3-airship case,  $0.6 \frac{m}{s}$  wind and stationary subject, which is part of Experiments 1, 2 and 3. There is good agreement between the predicted and actual flight trajectory in x and y directions. However, our model assumptions were too optimistic regarding the achievable vertical speed, and the simulated airships are less

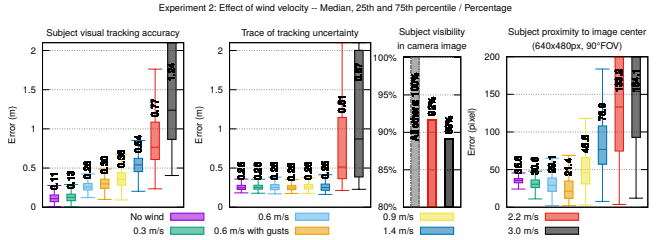


Fig. 11: Experiment 2: Effect of wind velocity.

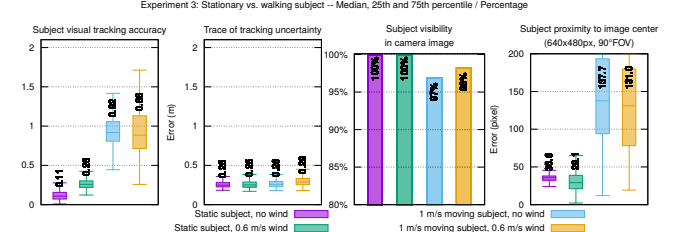


Fig. 12: Experiment 3: Subject not Stationary

agile in altitude than modeled. This is visible in the plots in the thin purple lines which represent the solver generated trajectories and suggests our choice for  $v_{v, \max} = 1.5 \frac{m}{s}$  needs to be reduced. However, this mismatch did not have a significant effect on the subject proximity to the camera image center, or on the tracking error.

### D. Experiment 2 - Wind Velocity

Figure 11 shows the effect of wind on the tracking formation with  $\|{}^F v\| = 0 \frac{m}{s}, 0.3 \frac{m}{s}, 0.6 \frac{m}{s}, 0.9 \frac{m}{s}, 1.4 \frac{m}{s}, 2.2 \frac{m}{s}$  and  $3.0 \frac{m}{s}$ . All evaluations were conducted with  $N = 3$  airships and a stationary subject. Up to  $1.4 \frac{m}{s}$  wind, there is a small but consistent decrease in tracking accuracy, however as the wind exceeds  $\frac{v_{\max} - v_{\min}}{4}$  (from  $\|{}^F v\| = 0.9 \frac{m}{s}$ ) the MPC no longer manages to keep subject  $S$  well centered in camera images. With  $\|{}^F v\| \geq 2.2 \frac{m}{s}$  the airships could no longer maintain sight of the subject through the entire orbit and with stronger wind there were increasingly large blind sectors during which  $S$  could not be observed. This also results in increased tracking error, although the subject was still visible in the cameras for close to 90% of all camera frames.

### E. Experiment 3 - Subject Not Stationary

Figure 12 shows the effect of subject motion. For two of the trials, with no wind and  $0.6 \frac{m}{s}$  wind, the subject is stationary, while for the third and fourth, the subject follows a repeated predefined trajectory. This subject path consists of straight and curved segments with sharp direction changes. This simulates the worst case described in Subsec. III-C. In the trials with moving subject, the subject velocity is  $\sim 1 \frac{m}{s}$ , which is much larger than  $\frac{v_{\max} - v_{\min}}{8}$ . Consequently, keeping the subject centered through the reversals is not possible. However, the MPC still maintains the subject in the camera FOV for 97% and 98% of all video frames in those trials, with or without wind. Typically only one out of three airships loses sight at a time and only for a very short time whenever an unanticipated subject direction change happens.

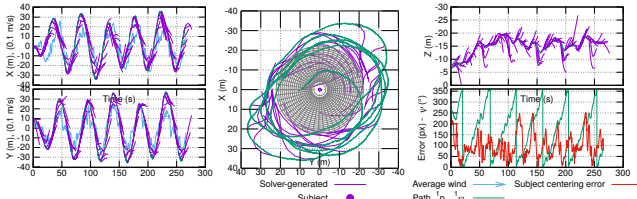


**Fig. 13:** Experiment 4: Real world flight. It was not possible to accurately estimate the wind in this flight, due to problems discussed in the text. Nevertheless, the MPC kept the simulated subject in the camera FOV at all times. The thin purple lines visible are the MPC predicted trajectories, which are not followed exactly due to errors in the model.

#### F. Experiment 4 - Real World Experiment

Figure 13 presents the trajectory of our real airship in an outdoor experiment. Here, we did not use visual tracking in the loop, but instead assumed a stationary subject at the origin. As in the simulation experiment, in Fig. 10, there is a good agreement between the predicted and actual trajectory in X and Y, but there is a larger mismatch in Z. The real airship rises or sinks as the MPC predicted, but with a lower vertical velocity. In the real world experiment, our algorithm was unable to correctly estimate the wind vector and the wind estimate is correlated with the position. We identified an erroneous in-flight state estimate of  $\psi_t$  as the cause for this mismatch. This highlights the susceptibility of our control approach to errors in state estimation. Nevertheless, as visible in the red plot in Fig. 13, the simulated subject remains in the camera image during the entire flight.

## V. CONCLUSION AND OUTLOOK

In this article, we presented an MPC-based method for formation control of airships with frame-fixed cameras. The goal of the MPC is to keep a moving subject within the field of view of the cameras of all the airships simultaneously, while adhering to other motion capture constraints. We derived analytical solutions in a simplified 2D case, boundary conditions on the subject velocity and approximate analytical solutions for realistic 3D case. Using these, we formulated it as an optimization problem and solved it using a numerical method. This was followed by an MPC implementation for real-time application. Through extensive simulations, we show our method's efficacy, accuracy and reliability. Through a real world demo we highlight that it is fast, stable and suited for real world application on airships. In future work, we will investigate the problem of collision and obstacle avoidance within the context of airship formation control. Generalization to other non-holonomic vehicles, e.g., fixed-wing aircrafts is also planned.

## REFERENCES

- [1] R. Tallamraju, E. Price, R. Ludwig, K. Karlapalem, H. H. Bülthoff, M. J. Black, and A. Ahmad, “Active perception based formation control for multiple aerial vehicles,” *IEEE Robotics and Automation Letters*, vol. 4, no. 4, pp. 4491–4498, Oct 2019.
- [2] R. Tallamraju, N. Saini, E. Bonetto, M. Pabst, Y. T. Liu, M. Black, and A. Ahmad, “Aircaprl: Autonomous aerial human motion capture using deep reinforcement learning,” *IEEE Robotics and Automation Letters*, vol. 5, no. 4, pp. 6678 – 6685, Oct. 2020, also accepted and presented in the 2020 IEEE/RSJ International Conference on Intelligent Robots and Systems (IROS).
- [3] N. Saini, E. Bonetto, E. Price, A. Ahmad, and M. J. Black, “AirPose: Multi-view fusion network for aerial 3D human pose and shape estimation,” *IEEE Robotics and Automation Letters*, vol. 7, no. 2, pp. 4805 – 4812, Apr. 2022, also accepted and presented in the 2022 IEEE International Conference on Robotics and Automation (ICRA).
- [4] E. Price, G. Lawless, R. Ludwig, I. Martinovic, H. H. Bülthoff, M. J. Black, and A. Ahmad, “Deep neural network-based cooperative visual tracking through multiple micro aerial vehicles,” *IEEE Robotics and Automation Letters*, vol. 3, no. 4, pp. 3193–3200, Oct 2018.
- [5] Y. T. Liu, E. Price, M. Black, and A. Ahmad, “Deep residual reinforcement learning based autonomous blimp control,” in *2022 IEEE/RSJ International Conference on Intelligent Robots and Systems (IROS)*. IEEE, Oct. 2022.
- [6] E. Price, Y. T. Liu, M. J. Black, and A. Ahmad, “Simulation and control of deformable autonomous airships in turbulent wind,” in *16th International Conference on Intelligent Autonomous System (IAS)*, June 2021.
- [7] L. Dubois and S. Suzuki, “Formation control of multiple quadcopters using model predictive control,” *Advanced Robotics*, vol. 32, no. 19, pp. 1037–1046, 2018.
- [8] K. Yamamoto, K. Sekiguchi, and K. Nonaka, “Experimental verification of formation control by model predictive control considering collision avoidance in three dimensional space with quadcopters,” in *2017 11th Asian Control Conference (ASCC)*, Dec 2017, pp. 1602–1607.
- [9] B. Lindqvist, P. Sopasakis, and G. Nikolakopoulos, “A scalable distributed collision avoidance scheme for multi-agent UAV systems,” in *Int Conf on Intelligent Robots and Systems (IROS)*, Sep-Oct 2021.
- [10] H. Fukushima, K. Kon, F. Matsuno, Y. Hada, K. Kawabata, and H. Asama, “Constrained model predictive control: Applications to multi-vehicle formation and an autonomous blimp,” in *2006 SICE-ICASE International Joint Conference*, Oct 2006, pp. 4515–4520.
- [11] E. Bicho, A. Moreira, S. Diegues, M. P. Carvalheira, and S. Monteiro, “Airship formation control,” in *3rd International Conference on Informatics in Control, Automation and Robotics - Workshop on Multi-Agent Robotic Systems (MARS 2006)*, 2006, pp. 22–33.
- [12] Z. He, J.-X. Xu, S. Yang, Q. Ren, and X. Deng, “On trackability of a moving target by fixed-wing uav using geometric approach,” in *2014 IEEE 23rd International Symposium on Industrial Electronics (ISIE)*, June 2014, pp. 1572–1577.
- [13] S. lin Liao, R. ming Zhu, N. qi Wu, T. A. Shaikh, M. Sharaf, and A. M. Mostafa, “Path planning for moving target tracking by fixed-wing uav,” *Defence Technology*, vol. 16, no. 4, pp. 811–824, 2020.
- [14] T. Z. Muslimov and R. A. Munasypov, “Multi-uav cooperative target tracking via consensus-based guidance vector fields and fuzzy mrac,” *Aircraft Engineering and Aerospace Technology*, vol. 93, no. 7, pp. 1204–1212, Jan 2021.
- [15] M. Zhang and H. H. T. Liu, “Cooperative tracking a moving target using multiple fixed-wing uavs,” *Journal of Intelligent & Robotic Systems*, vol. 81, no. 3, pp. 505–529, Mar 2016.
- [16] T. Z. Muslimov and R. A. Munasypov, “Coordinated uav standoff tracking of moving target based on lyapunov vector fields,” in *2020 International Conference Nonlinearity, Information and Robotics (NIR)*, Dec 2020, pp. 1–5.
- [17] T. Von Kármán, *Aerodynamics*, ser. McGraw-Hill paperbacks : science, mathematics and engineering. McGraw-Hill, 1963.
- [18] P. Sopasakis, E. Fresk, and P. Patrinos, “OpEn: Code generation for embedded nonconvex optimization,” in *IFAC World Congress*, Berlin, Germany, 2020.
- [19] L. Stella, A. Themelis, P. Sopasakis, and P. Patrinos, “A simple and efficient algorithm for nonlinear model predictive control,” in *IEEE Conference on Decision and Control (CDC)*, Dec 2017, pp. 1939–1944.
- [20] W. Liu, D. Anguelov, D. Erhan, C. Szegedy, S. Reed, C.-Y. Fu, and A. C. Berg, “Ssd: Single shot multibox detector,” in *Computer Vision – ECCV 2016*, B. Leibe, J. Matas, N. Sebe, and M. Welling, Eds. Cham: Springer International Publishing, 2016, pp. 21–37.